Study of optical clearing in polarization measurements by Monte Carlo simulations with anisotropic tissue-mimicking models

Dongsheng Chen
Nan Zeng
Yunfei Wang
Honghui He
Valery V. Tuchin
Hui Ma

SPIE.

Study of optical clearing in polarization measurements by Monte Carlo simulations with anisotropic tissue-mimicking models

Dongsheng Chen,[a,b] Nan Zeng,[a] Yunfei Wang,[a,b] Honghui He,[b] Valery V. Tuchin,[c,d,e,]* and Hui Ma[a,b,]*

[a]Tsinghua University, Graduate School at Shenzhen, Institute of Optical Imaging and Sensing,
Shenzhen Key Laboratory for Minimal Invasive Medical Technologies, 2279 Lishui Road, Shenzhen 518055, China
[b]Tsinghua University, Department of Physics, 30 Shuangqing Road, Beijing 100084, China
[c]Saratov State University, Research-Educational Institute of Optics and Biophotonics, 83 Astrakhanskaya Street, Saratov 410012, Russia
[d]Tomsk State University, Laboratory of Biophotonics, 36 Lenin Avenue, Tomsk 634050, Russia
[e]Institute of Precision Mechanics and Control of RAS, 24 Rabochaya Street, Saratov 410028, Russia

Abstract. We conducted Monte Carlo simulations based on anisotropic sclera-mimicking models to examine the polarization features in Mueller matrix polar decomposition (MMPD) parameters during the refractive index matching process, which is one of the major mechanisms of optical clearing. In a preliminary attempt, by changing the parameters of the models, wavelengths, and detection geometries, we demonstrate how the depolarization coefficient and retardance vary during the refractive index matching process and explain the polarization features using the average value and standard deviation of scattering numbers of the detected photons. We also study the depth-resolved polarization features during the gradual progression of the refractive index matching process. The results above indicate that the refractive index matching process increases the depth of polarization measurements and may lead to higher contrast between tissues of different anisotropies in deeper layers. MMPD-derived polarization parameters can characterize the refractive index matching process qualitatively. © *2016 Society of Photo-Optical Instrumentation Engineers (SPIE)* [DOI: 10.1117/1.JBO.21.8.081209]

1 Introduction

Optical clearing (OC) reduces scattering and improves the imaging depth, resolution, and contrast. It may find wide applications in areas of biomedical imaging.[1–9] For example, imaging of three-dimensional microstructure of whole tissue, such as brain and central nervous system, has been realized recently with an unprecedented resolution through combination of OC technique with advanced microscopy imaging and labeling techniques.[2,10] One of the main mechanisms of OC is the refractive index matching between the scattering particles and the surrounding interstitial medium.[11] Polarization measurements are sensitive to tissues' structural and optical properties, such as the scattering coefficient, size and shape of the scatterers, birefringence, and optical activity of the interstitial medium, and so on. Especially, recently with the progress of imaging techniques and analysis methods Mueller matrix polarimetry develops rapidly.[12] Mueller matrix polar decomposition (MMPD) proposed by Lu and Chipman is prevalently used, by which we can decouple different polarization effects and extract several physically meaningful polarization parameters that have been widely applied in the analysis of polarization-related properties of tissues.[13–16] But due to multiple scattering in turbid tissues, the polarimetry imaging depth is usually low and the intrinsic structural properties may be undetected. OC techniques, which reduce scattering, are predicted to be very useful in the polarization measurements, such as Mueller matrix polarimetry.

In this paper, as a preliminary attempt, we study the polarization features in the MMPD parameters during the refractive index matching process using Monte Carlo simulations based on anisotropic tissue-mimicking scattering models. By changing the parameters of the models, wavelengths, and detecting geometries, we get a relatively systematic knowledge and understanding of polarization features during the refractive index matching process and the ability of polarization methods in characterizing the refractive index matching processes.

2 Method

In order to analyze the scattering and polarization properties of anisotropic media, we proposed a sphere–cylinder birefringence model (SCBM)[17–19] and corresponding Monte Carlo simulation programs, which have been successfully applied in many previous studies.[20,21] The SCBM consists of three key components: spherical scatterers, infinitely long cylindrical scatterers, and a birefringent interstitial medium. The cylindrical scatterers can be used to represent fibrous structures, such as collagen and elastin, while the spherical scatterers can be used for mimicking structures, such as the cell nuclei and organelles. Different models can be developed by various combinations of the two types of scatterers and birefringent interstitial medium according to the characteristics of tissues under study.

There have been numerous studies on the microstructure of the sclera tissue. The sclera mainly consists of long collagen fibrils with variable diameters, which form lamellar bundles.[1]

*Address all correspondence to: Hui Ma, E-mail: mahui@tsinghua.edu.cn;
Valery V. Tuchin, E-mail: tuchinvv@mail.ru

There are occasionally large empty spaces between the bundles. Elastic fibers and microfibrils are occasionally found between the collagen bundles.[22] There also exist proteoglycan filaments in association with the collagen d-band throughout all levels of the sclera, and the filaments appear in three orientations.[23,24] In accordance with the structural properties of the sclera tissue, we build a sclera model using the sphere–cylinder scattering model (SCSM), as shown in Fig. 1. In the model, cylindrical scatterers represent long collagen fibrils, and spherical scatterers account for the inclusion of short collagen fibrils randomly distributed among basic aligned, much longer fibrils, the proteoglycans, distributed between the collagen bundles, and cell organelles. The ratio between scattering coefficients induced by spherical scatterers and cylindrical scatterers (represented by S/C) is varied to create systems of different anisotropy degrees.

Here, we study by Monte Carlo simulation the refractive index matching mechanism of OC, which causes the changes of the scattering properties of both types of scatterers. Monte Caro simulation is a stochastic numerical method widely applied in biomedical optics. In the simulation, we track the directions, locations, and polarization states of the photons, which are statistically transmitted in the sample, and collect the information of the photons when they leave the sample. The number of photons for each simulation is 10^7. Through several simulations with different incident polarization states, the Mueller matrix of the sample is obtained, and then analyzed with the MMPD method to get polarization parameters. Here, we use the Lu–Chipman MMPD method[13] to decompose the Mueller matrix into a product of three submatrices, depolarization matrix (M_Δ), retardation matrix (M_R), and diattenuation matrix (M_D) as

$$M = M_\Delta \cdot M_R \cdot M_D. \tag{1}$$

Depolarization coefficient Δ, retardation δ, and diattenuation coefficient D are derived from each matrix, respectively.

First, we study the uniformly refractive index matching process of the whole sample with a single-layer sclera model. The parameters used in the simulations are the diameters of S/C, 50 and 100 nm, respectively. The refractive index of both types of scatterers is 1.474, while that of the interstitial medium n_m is 1.35 before OC and gradually increases to 1.45 by 0.02 for every step of the clearing process in the simulation. The thickness of the medium is 0.1 cm. The wavelengths of incident light λ are 600 and 800 nm. For incident wavelength of 600 nm, the initial scattering coefficient is 100/cm and the initial absorption coefficient is 0/cm before clearing.[1] To study the gradual refractive index matching process with depth, we use a three-layer sclera scattering model. In this model, the thicknesses are
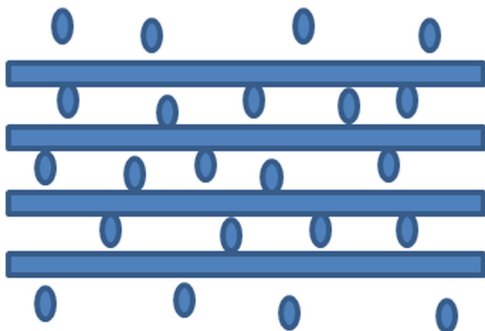
0.033, 0.033, and 0.034 cm, respectively, from the top layer to the bottom one. The process of the refractive index matching is divided into four stages with the refractive indexes of the three layers as 1.37, 1.36, 1.35 (corresponding to the top layer, the middle layer, and the bottom layer), 1.40, 1.39, 1.38; 1.43, 1.42, 1.41; and 1.45, 1.44, 1.43 in turn. The stages are represented by n_c, which is assigned from 1 to 4 in turn. The different layers are represented by z_c from 1 to 3 from the top layer to the bottom one. To mimic Mueller matrix imaging with wide-field illumination, we use a pencil beam for illumination and record scattered photons over a 1×1 cm area in both the forward and backward detection geometries.

By analysis of the transmission characteristics of the detected photons, such as the average value and standard deviation of scattering numbers, we try to illustrate the polarization features during the refractive index matching process.

3 Results and Discussions

First, we conducted the study of the uniformly refractive index matching process of the whole tissue with a single-layer sclera model. The distributions of scattering numbers of detected photons in forward and backward detection geometries are shown in Figs. 2–4, with different refractive indexes of the interstitial medium and degrees of anisotropy represented by the ratio of scattering coefficients induced by the S/C. The incident wavelength is 600 nm. The incident light is horizontally linearly polarized. The results with other incident polarizations are similar, so are not listed. For different degrees of anisotropy, it is observed that during the refractive index matching process the ratio of intensities between the forward and backward detections increases and the average scattering number in both directions decreases. The number of forward-detected photons decreases with S/C value. From above, the changes of distributions of scattering numbers during the refractive index matching process indicate a reduction of scattering by the refractive index matching and are closely related to the acquired polarization features illustrated in Sec. 4.

Then, we studied the relations between the polarization parameters derived from the Lu–Chipman MMPD method and the refractive index of the interstitial medium for samples of variable anisotropy degrees in both forward and backward detection configurations with incident wavelength of 600 nm, as shown in Figs. 5 and 6.

In this study, the diattenuation values derived from MMPD are <0.04, which induce much weaker effects compared to those due to depolarization and retardance. So diattenuation is neglected in this paper.

For the forward detection configuration as shown in Fig. 5, the depolarization coefficient decreases with the increasing refractive index of the interstitial medium or better refractive index matching. The scattering number of the detected photons also decreases as the sample becomes more transparent. For the sample of higher S/C value, the depolarization coefficient is slightly larger due to higher depolarizing ability of the smaller sphere than the thicker cylinder. The retardance also decreases with the improved refractive index matching. It has been indicated from a previous study that well-aligned cylindrical scatterers can generate retardance by Ref. 16, which increases as the proportion of aligned cylindrical scatterers increases. Figure 5 does show that the retardance goes down with the increase of S/C value and with the decrease of scattering number due to the refractive index matching. It should be noted that the
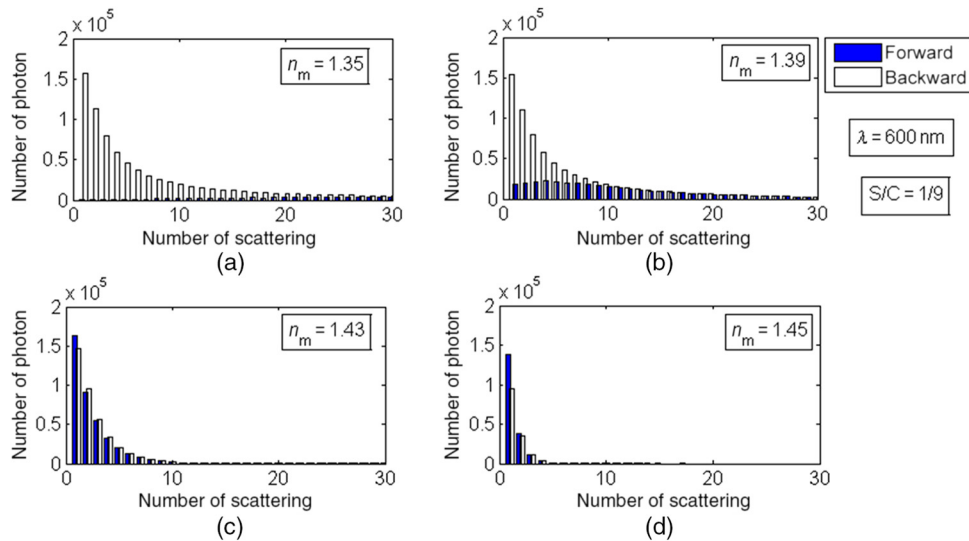

Fig. 1 The sketch map for SCSM.

Fig. 2 For highly isotropic single-layer sclera sample (the ratio between scattering coefficients induced by S/C = 9/1), the distribution of scattering number of forward and backward detected light for different refractive indexes of the interstitial medium n_m. (a) $n_m = 1.35$, (b) $n_m = 1.39$, (c) $n_m = 1.43$, and (d) $n_m = 1.45$.
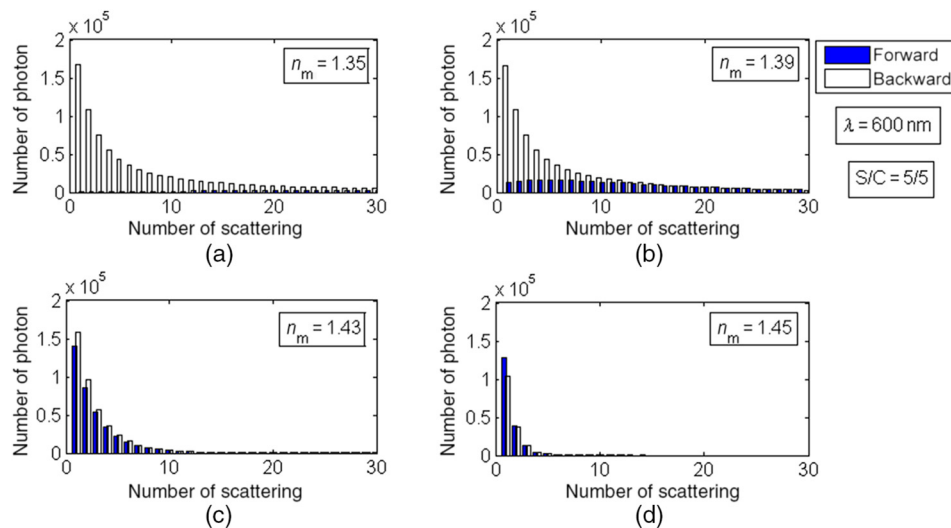

Fig. 3 For anisotropic single-layer sclera sample (S/C = 5/5), the distribution of scattering number of forward and backward detected light for different refractive indexes of the interstitial medium n_m. (a) $n_m = 1.35$, (b) $n_m = 1.39$, (c) $n_m = 1.43$, and (d) $n_m = 1.45$.

first points of red circle and green square in Fig. 5(b), which correspond to nearly isotropic samples (S/C = 9/1 and 7/3) at insufficient refractive index matching, are incorrect because retardance is not well defined at very large scattering numbers [Fig. 5(c)] and too prominent depolarization [Fig. 5(a)] for samples of low anisotropy.

For the backward detection configuration, the results are shown in Fig. 6. The depolarization coefficient decreases during the refractive index matching process, as shown in Fig. 6(a). The retardance detected in the backward configuration is also due to scattering by cylinders, therefore, decreasing with the increasing S/C values and the refractive index matching. These results are due to the limited thickness of sample and detection area. When the thickness and detection area are large enough, e.g., the thickness is 5 cm and detection area is 10 × 10 cm for a sample of S/C values equal to 5/5, the depolarization coefficient and retardance almost stay constant during the refractive index matching process, shown as the dotted lines in Figs. 6(a) and 6(b). The average depth and transverse range traveled by the backward-detected photons are inversely proportional to the scattering coefficient but the scattering numbers of both types of scatterers stay constant during the refractive index matching process when the thickness of sample and detection area are large enough.

For both detection configurations, as the average value and standard deviation of scattering number get smaller, the changing rates of the depolarization coefficient and retardance with the refractive index matching increase, as shown in Figs. 5 and 6. For the same sample, the magnitudes and changes of MMPD parameters with the refractive index matching are bigger in the forward detection configuration due to larger scattering number, as shown in Figs. 5 and 6.
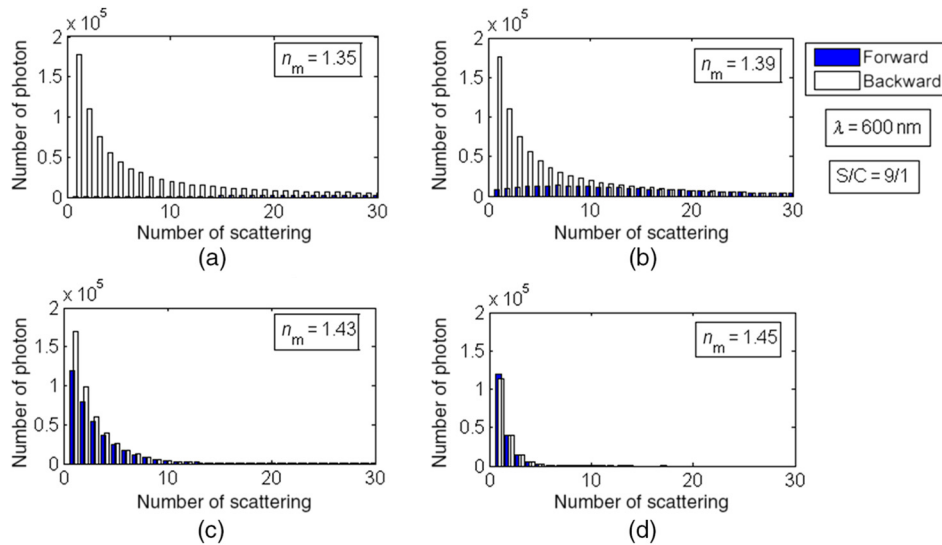
Fig. 4 For highly anisotropic single-layer sclera sample (S/C = 1/9), the distribution of scattering number of forward and backward detected light for different refractive indexes of the interstitial medium n_m. (a) $n_m = 1.35$, (b) $n_m = 1.39$, (c) $n_m = 1.43$, and (d) $n_m = 1.45$.
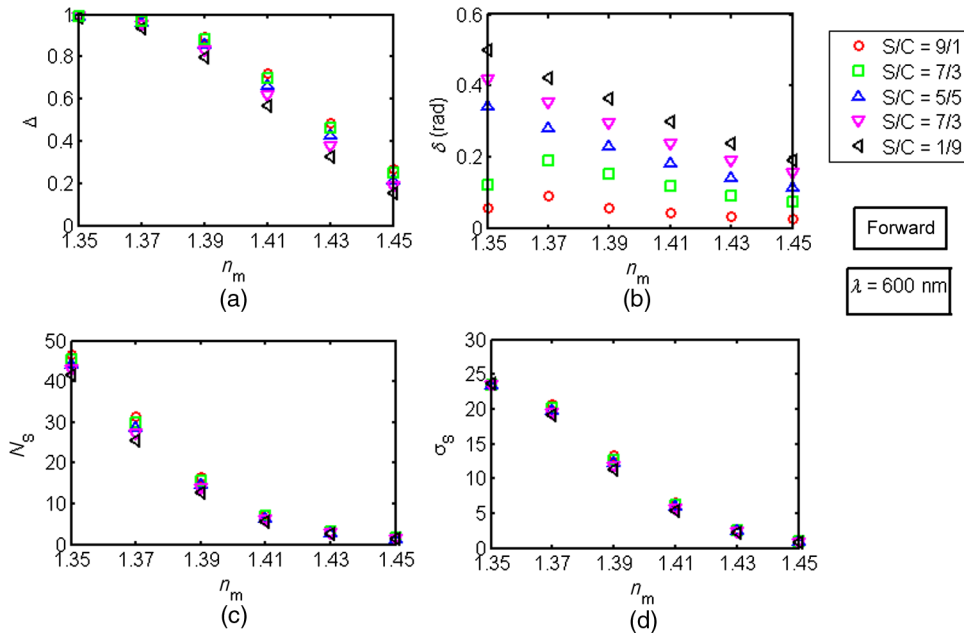

Fig. 5 The single-layer sclera model for the forward configuration with incident wavelength of 600 nm. MMPD parameters, the average value, and standard deviation of scattering numbers change with the refractive index of the interstitial medium during the refractive index matching process. (a) Depolarization coefficient Δ, (b) retardance δ, (c) average value of scattering number N_S, and (d) standard deviation of scattering number σ_S.

Both scattering-induced depolarization and cylindrical scatterers-induced retardance are positively correlated to the corresponding scattering number.

For comparison among different incident wavelengths, simulations with 800-nm wavelength illumination in both forward and backward detection configurations are shown in Figs. 7 and 8.

For the forward detection configuration, as the refractive index matching process progresses, the depolarization coefficients of samples of different anisotropy degrees decline and the discrepancy among the samples increases weakly, as shown in Fig. 7(a), due to the decrease of scattering number of both types of scatterers. The values of retardance for the samples also decrease with the refractive index matching, due to the decrease of scattering number by cylindrical scatterer. The retardance decreases with the increasing S/C value as the scattering number by cylindrical scatterer decreases. The discrepancy of retardances between samples of different anisotropy degrees declines with the refractive index matching due to the decrease of the difference of scattering number by cylindrical scatterers among the samples, as shown in Fig. 7(c).
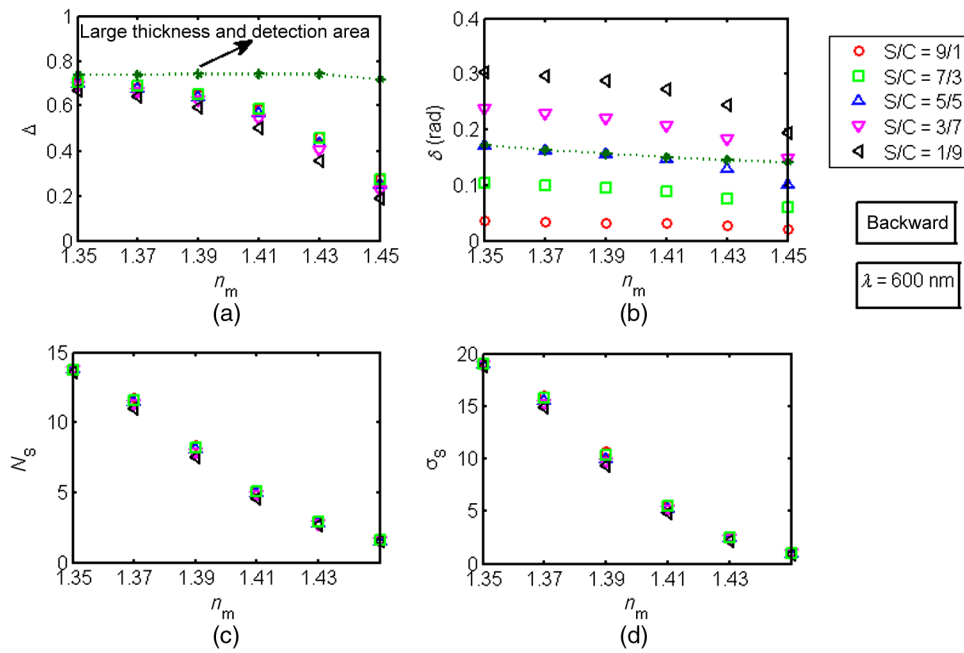
Fig. 6 The single-layer sclera model for the backward configuration with incident wavelength of 600 nm. MMPD parameters, the average value, and standard deviation of scattering numbers change with the refractive index of the interstitial medium during the refractive index matching process. (a) Depolarization coefficient Δ, (b) retardance δ, (c) average value of scattering number N_S, and (d) standard deviation of scattering number σ_S.
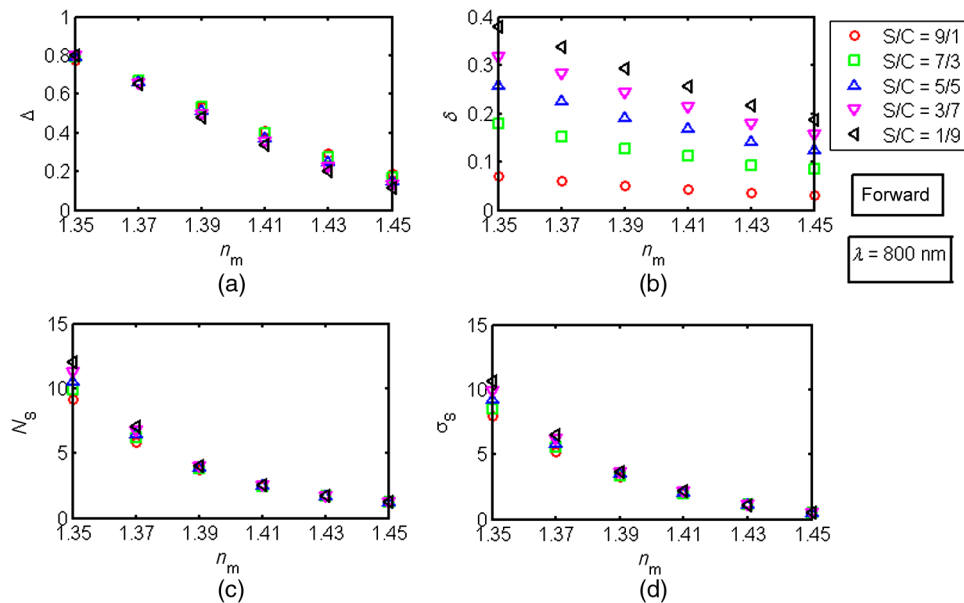

Fig. 7 The single-layer sclera model for the forward configuration with the incident wavelength of 800 nm. MMPD parameters, the average value, and standard deviation of scattering numbers change with the refractive index of the interstitial medium in the refractive index matching process. (a) Depolarization coefficient Δ, (b) retardance δ, (c) average value of scattering number N_S, and (d) standard deviation of scattering number σ_S.

For the backward detection configuration, the depolarization coefficients of different samples decline during the refractive index matching process, as shown in Fig. 8(a), due to the decrease of the scattering number as shown in Figs. 8(c) and 8(d). The values of retardance for the samples of different anisotropy degrees decrease as the clearing process progresses,

as shown in Fig. 8(b), because the scattering number by the cylindrical scatterer goes down. The discrepancy of the values of retardance among the samples declines because the difference of the scattering number by cylindrical scatterer among the samples decreases. Here, the change of the depolarization coefficients and retardance with the refractive index matching in
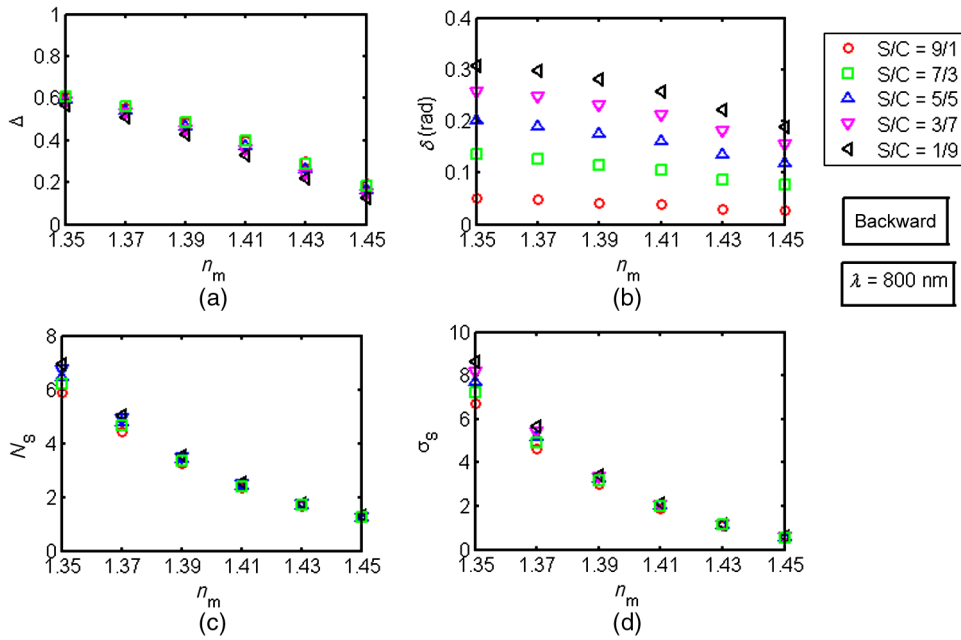
Fig. 8 The single-layer sclera model for the backward configuration with the incident wavelength of 800 nm. MMPD parameters, the average value, and standard deviation of scattering numbers change with the refractive index of the interstitial medium in the refractive index matching process. (a) Depolarization coefficient Δ, (b) retardance δ, (c) average value of scattering number N_S, and (d) standard deviation of scattering number σ_S.

backward detection configuration is also due to the limited thickness of sample and detection area. When the thickness and detection area are large enough, the two polarization parameters will stay constant, just as the results with the incident wavelength of 600 nm.

There are differences between the results of 600- and 800-nm incident wavelengths. In general, the values of MMPD parameters for 800 nm are smaller, which are due to the smaller scattering number. This is because the depolarization is induced by scattering of both types of scatterers and
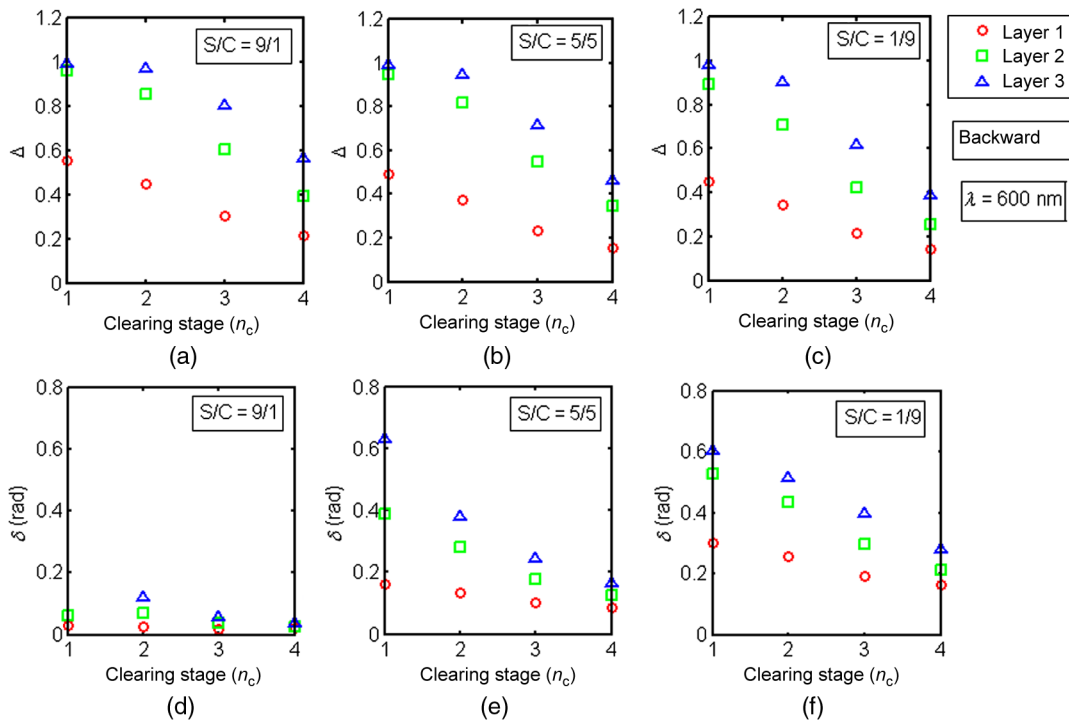

Fig. 9 The three-layer sclera model for the backward configuration with the incident wavelength of 600 nm, MMPD parameters change with stages of index matching n_c, with different markers representing different layers, the ratios of scattering coefficients induced by S/C are 9/1, 5/5, and 1/9, respectively, from left to right. (a)–(c) are depolarization coefficients Δ and (d)–(f) are retardances δ.

retardance by scattering of the cylindrical scatterer; both MMPD parameters are positively related to the corresponding scattering number. The change of MMPD parameters for a wavelength of 800 nm, especially the depolarization coefficient in the backward detection configuration, is more obvious than those for 600 nm in the initial stage of the refractive index matching. This is due to the faster change of polarization parameters with the refractive index matching when scattering numbers are small in both detection configurations, as shown in Figs. 5 and 6.

Further, we consider the gradual progression of the refractive index matching process with depth, using a three-layer sclera model with gradually changing refractive index matching for different layers.

First, we analyze the information of photon backscattered from different layers and obtain the MMPD parameters at different clearing stages for each layer, as shown in Fig. 9. From the curves, we can observe that for each layer, whose curves are marked by different symbols, the regularities of both depolarization coefficient and retardance with clearing stages are similar to those with the single-layer model. The effect of the refractive index matching on the polarization parameters is larger in the deeper layer due to larger distances traveled by photons from the deeper layer; meanwhile, the discrepancy of polarization parameters among different layers decreases with the increasing refractive index matching as the whole sample gets more and more transparent. The decrease of depolarization coefficient with the refractive index matching indicates that the refractive index matching process can increase the imaging depth of polarization measurements. It should be noted that the incorrect retardance in the upper triangle in

Fig. 9(d), which is unseen in the figure, is due to too prominent depolarization.

Then, we change the description of the results as shown in Fig. 9 and obtain curves of polarization parameters with depth represented by layer number z_c for different clearing stages, shown in Fig. 10. It can be observed that the trend of polarization parameters with depth gets more and more linear with clearing stages, indicating that the retardance effect of cylindrical scattering approaches the effect of birefringence during the refractive index matching process. By comparison of Figs. 10(a), 10(b), and 10(c), it is observed that the contrast of depolarization coefficients for samples of different anisotropy degrees in the deep layer increases obviously with the improved refractive index matching, making it possible to differentiate the samples of different anisotropy degrees in deep layers with polarization methods. It also indicates the improvement of polarization imaging depth by the refractive index matching. The incorrect retardance in the upper triangle in Fig. 10(d), which is unseen in the figure, is due to too prominent depolarization.

4 Discussion

It has been demonstrated that in backscattering geometry the Mueller matrix-derived retardance parameters may connect to the medium optical properties in a rather complex way and may vary with the detection geometry.[25] The effect of scattering-induced linear retardance on the intrinsic retardance is significant when the detection point is within the transport length $(1/\mu_s')$ to the illumination point, while the effect is much smaller outside the transport length. In this work, the transport length varies from 0.01 to 0.5 cm due to index matching, which can
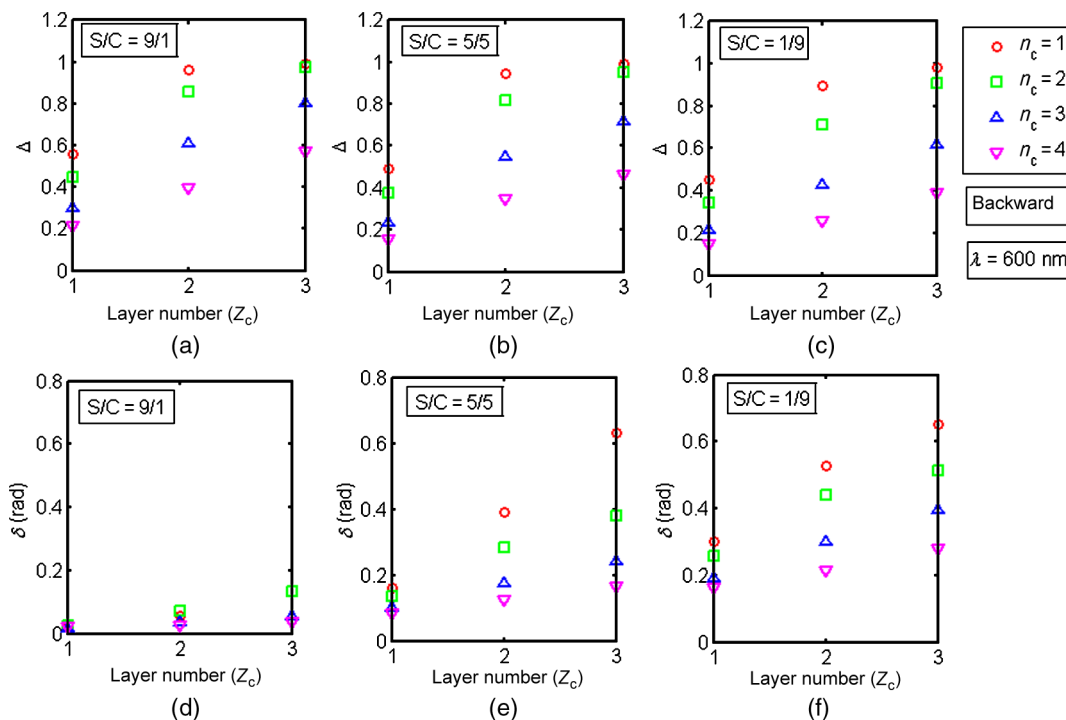

Fig. 10 Corresponding to Fig. 9, MMPD parameters change with the depth number z_c, with different markers representing different clearing stages n_c, the ratios of scattering coefficients induced by S/C are 9/1, 5/5, and 1/9, respectively, from left to right. (a)–(c) are depolarization coefficients Δ and (d)–(f) are retardances δ.

be comparable to the 1×1 cm detection area. In order to verify the influence of scattering-induced linear retardance on the intrinsic retardance, we repeat some simulations with 1×1 mm detected area. The results show that the retardance values differ by <15% and the dependence of retardances on index matching follows the same trend. Therefore, the present simulations for wide-field illuminations are not sensitive to the detection geometry.

In the present study, all the results are obtained using the Lu–Chipman MMPD method. Due to the noncommuting nature of matrix multiplication, there are two groups of MMPD decomposition methods depending on the order between the depolarization and the diattenuation matrices.[26,27] There are also more general decomposition methods, which do not suffer from the multiplication order ambiguity, such as the pseudopolar decomposition method.[28] However, the Lu–Chipman method is widely adopted since it always leads to physical elementary matrices.[26] The differences between the two groups of decomposition are negligible for weak diattenuation.[27] In this work, the Mueller matrix-derived diattenuation value is 0.04 for the Lu–Chipman method. If we reverse the order between the depolarization and diattenuation matrices, the diattenuation value without index matching changes to 0.4, but decreases to <0.05 as the index matching progresses. The trends for the depolarization coefficients and retardances during index matching stay the same for the two forms of decompositions. The values differ by <10% and reduce to almost zero when the index matching degree is very large.

5 Conclusion

We study the polarization features during the process of the refractive index matching using Monte Carlo simulations based on sclera-mimicking models by changing the anisotropy of the samples, incident wavelengths, detection configurations, and so on. The depolarization coefficient and retardance derived from MMPD relate regularly with the degree of the refractive index matching. The refractive index matching process suppresses scattering in both forward and backward detection configurations, reducing the depolarization by scattering of both types of scatterers, and the retardance induced by cylindrical scatterers. It also indicates that OC can improve the contrast of the acquired polarization parameters among samples of different anisotropies and the imaging depths of polarization measurements. Also, the MMPD-derived polarization parameters can characterize the refractive index matching process qualitatively. Therefore, from the preliminary study shown in this paper, we predict that OC technique is potentially useful in polarimetry, and polarization methods in turn are potentially powerful tools to characterize OC mechanisms and processes in some tissue models, including muscle tissue, where myofibrils and spherical mitochondria are the main scatterers.

References

1. V. V. Tuchin, *Tissue Optics: Light Scattering Methods and Instruments for Medical Diagnosis*, 3rd ed., p. 986, SPIE Press, Bellingham, Washington (2015).
2. D. Zhu et al., "Recent progress in tissue optical clearing," *Laser Photonics Rev.* **7**(5), 732–757 (2013).
3. A. Bykov et al., "Imaging of subchondral bone by optical coherence tomography upon optical clearing of articular cartilage," *J. Biophotonics* **9**, 270–275 (2015).
4. J. Wang et al., "Review: tissue optical clearing window for blood flow monitoring," *IEEE J. Sel. Top. Quantum Electron.* **20**(2), 92–103 (2014).
5. S. Plotnnikov et al., "Optical clearing for improved contrast in second harmonic generation imaging of skeletal muscle," *Biophys. J.* **90**(1), 328–339 (2006).
6. S. G. Proskurin and I. V. Meglinski, "Optical coherence tomography imaging depth enhancement by superficial skin optical clearing," *Laser Phys. Lett.* **4**(11), 824–826 (2007).
7. S. Eunjoo et al., "Optical clearing based cellular-level 3D visualization of intact lymph node cortex," *Biomed. Opt. Express* **6**(10), 4154–4164 (2015).
8. V. V. Tuchin, L. Wang, and D. A. Zimnyakov, *Optical Polarization in Biomedical Applications*, p. 275, Springer-Verlag, Berlin, Heidelberg, New York (2006).
9. C. Macdonald and I. Meglinski, "Backscattering of circular polarized light from a disperse random medium influenced by optical clearing," *Laser Phys. Lett.* **8**(4), 324–328 (2011).
10. H. Hama et al., "Scale: a chemical approach for fluorescence imaging and reconstruction of transparent mouse brain," *Nat. Neurosci.* **14**(11), 1481–1488 (2011).
11. V. V. Tuchin, "Optical clearing of tissues and blood using the immersion method," *J. Phys. D: Appl. Phys.* **38**(15), 2497–2518 (2005).
12. N. Ghosh and I. A. Vitkin, "Tissue polarimetry: concepts, challenges, applications, and outlook," *J. Biomed. Opt.* **16**(11), 110801 (2011).
13. S. Lu and R. Chipman, "Interpretation of Mueller matrices based on polar decomposition," *J. Opt. Soc. Am. A* **13**(5), 1106–1113 (1996).
14. S. Manhas et al., "Mueller matrix approach for determination of optical rotation in chiral turbid media in backscattering geometry," *Opt. Express* **14**(1), 190–202 (2006).
15. M. F. G. Wood, X. Guo, and I. A. Vitkin, "Polarized light propagation in multiply scattering media exhibiting both linear birefringence and optical activity: Monte Carlo model and experimental methodology," *J. Biomed. Opt.* **12**(1), 014029 (2007).
16. Y. Guo et al., "A study on forward scattering Mueller matrix decomposition in anisotropic medium," *Opt. Express* **21**(15), 18361–18370 (2013).
17. T. Yun et al., "Monte Carlo simulation of polarized photon scattering in anisotropic media," *Opt. Express* **17**(19), 16590–16602 (2009).
18. H. He et al., "Application of sphere–cylinder scattering model to skeletal muscle," *Opt. Express* **18**(14), 15104–15112 (2010).
19. E. Du et al., "Two dimensional backscattering Mueller matrix of sphere–cylinder birefringence media," *J. Biomed. Opt.* **17**(12), 126016 (2012).
20. E. Du et al., "Mueller matrix polarimetry for differentiating characteristic features of cancerous tissues," *J. Biomed. Opt.* **19**(7), 076013 (2014).
21. C. He et al., "Characterizing microstructures of cancerous tissues using multispectral transformed Mueller matrix polarization parameters," *Biomed. Opt. Express* **6**(8), 2934–2945 (2015).
22. Y. Kamai and T. Ushiki, "The three-dimensional organization of collagen fibrils in the human cornea and sclera," *Invest. Ophthalmol. Vis. Sci.* **32**(8), 2244–2258 (1991).
23. R. D. Young, "The ultrastructural organization of proteoglycans and collagen in human and rabbit sclera matrix," *J. Cell Sci.* **74**(3), 95–104 (1985).
24. J. A. Rada et al., "Proteoglycans in the human sclera. Evidence for the presence of aggrecan," *Invest. Ophthalmol. Vis. Sci.* **38**(9), 1740–1751 (1997).
25. N. Ghosh, M. F. G. Wood, and I. A. Vitkin, "Polarimetry in turbid, birefringent, optically active media: a Monte Carlo study of Mueller matrix

decomposition in the backscattering geometry," *J. Appl. Phys.* **105**(10), 102023 (2009).

26. J. Morio and F. Goudail, "Influence of the order of diattenuator, retarder, and polarizer in polar decomposition of Mueller matrices," *Opt. Lett.* **29**(19), 2234–2236 (2004).

27. N. Ghosh, M. F. G. Wood, and I. A. Vitkin, "Influence of the order of the constituent basis matrices on the Mueller decomposition-derived polarization parameters in complex turbid media such as biological tissues," *Opt. Commun.* **283**(6), 1200–1208 (2010).

28. O. Arteaga and A. Canillas, "Pseudopolar decomposition of the Jones and Mueller-Jones exponential polarization matrices," *J. Opt. Soc. Am. A* **26**(4), 783–793 (2009).

Biographies for the authors are not available.